Supporting Information:

N, S co-doped $V_3Nb_{17}O_{50}$@C fibers used for lithium- ion storage

Hongliang Fu [a], Qi Duan [a], Yue Lian [a], Dawei Wang [a], Yongqing Bai [a], Zonglun Cao [b], Jie Sun [b], Jing Zhao [a], Huaihao Zhang [a,*]

[a] School of Chemistry & Chemical Engineering, Yangzhou University, Yangzhou 225002, PR China

[b] SINOPEC Beijing Research Institute of Chemical Industry, Beijing 100013, PR China

Experimental section

Synthesis of $V_3Nb_{17}O_{50}$ precursor

NH_4VO_3 (1.5 mmol, 99%) and $NbCl_5$ (8.5 mmol, 99.9%) were dissolved in 60 mL isopropyl alcohol successively and stirred at room temperature for 4 h to form a homogeneous solution. The obtained solution was transferred into a Teflon-lined autoclave (100 mL) and kept at 200 ℃ for 24 h. After cooling down naturally, the precipitate was collected by centrifugation, washed with deionized water and ethanol individually, and dried at 80 ℃ for 12 h in a vacuum oven.

Synthesis of $V_3Nb_{17}O_{50}$@NC and S-$V_3Nb_{17}O_{50}$@NC

$V_3Nb_{17}O_{50}$ precursor (0.6g), PAN (0.2 g, Mw = 15000), and DMF (2 mL) were added to a beaker, and stirred in a 60 ℃ water bath for 10 h to acquire the precursor solution. Then, the precursor solution was transferred to a syringe with a 21 G needle (inner diameter = 0.5 mm), and spun into nanofibers under such condition: a voltage of 16 kV, a speed of 0.1 mL h^{-1}, and a distance of 15 cm between the needle and the plate. The spun fibers were cured at 200 ℃ for 2 h, then kept at 800 ℃ for 2 h in a tubular furnace in N_2 atmosphere at a heating rate of 2 ℃ min^{-1}, thus to obtain $V_3Nb_{17}O_{50}$@NC (the contrast sample). After that, $V_3Nb_{17}O_{50}$@NC mixed with sublimated sulfur in a mass ratio of 1:5 were placed in the tubular furnace, and hold at 500 ℃ for 2 h at a heating rate of 2 ℃ min^{-1} under N_2 atmosphere to acquire S-$V_3Nb_{17}O_{50}$@NC.

Material characterization

The composition and purity of the obtained samples were characterized by X-ray powder diffraction (XRD, Bruker, D8 super speed, Germany) with Cu Kα radiation (λ = 1.5406 Å). The Raman spectra of products were recorded using a Raman spectrometer (Renishaw Invia) at 532 nm laser wavelength. The morphology and microstructure were observed by scanning electron microscopy (FESEM, Hitachi, S-4800 II, Japan) and transmission electron microscopy (TEM, Philips, TECNAI 12, Holland). The lattice parameters of samples were determined by high-resolution transmission electron microscopy (HRTEM, Tecnai, G2F30 S-TWIN, USA) equipped with an energy dispersive X-ray spectrometer (EDS). Surface analysis of samples were carried out by X-ray photoelectron spectroscopy (XPS, Thermo Science, ESCALAB

250Xi, USA). The carbon content of the samples was available by thermogravimetric analysis (Pyris 1 TGA, PerkinElmer) from room temperature to 800 °C at a rate of 5 °C min^{-1} in the air atmosphere.

Electrochemical measurements

Electrochemical tests were attainable on $V_3Nb_{17}O_{50}$@NC and S-$V_3Nb_{17}O_{50}$@NC electrodes using half-cell and full-cell. $V_3Nb_{17}O_{50}$@NC/S-$V_3Nb_{17}O_{50}$@NC (the active material, 80 wt%), acetylene black (the conductive agent, 10 wt%), and polyvinylidene fluoride (PVDF, the binder, 10 wt%) were homogeneously mixed in N-methyl-2-pyrrolidone (NMP). The resulting slurries were coated on Cu foil, dried overnight at 80 °C, and then roll-pressed (with ~ 1 mg cm^{-2} mass loading of the active material). The half-cell tests were carried out using 2032-type coin cells with Li metal as anode, S-$V_3Nb_{17}O_{50}$@NC as cathode, 1.0 M $LiPF_6$ in ethylene carbonate/dimethyl carbonate (EC/DMC, 1:1) as electrolyte, and polypropylene membrance (Celgard 2400) as separator. All coin cell assembly steps were operated in an Ar-filled glove box. For LIC, the activated carbon (AC) cathode was prepared using Al foil as current collector in the same way as mentioned above. S-$V_3Nb_{17}O_{50}$@NC was employed as anode and activated carbon as cathode. The mass ratio of cathode to anode was controlled at about 3.6:1 in the voltage range of 0.5–3.0 V. The galvanostatic charge/discharge (GCD) performances of LIB and LIC were available on a Neware Battery Tester. Cyclic voltammetry (CV) measurements were acquired on a CHI 660E electrochemical workstation.

Fig. S1. Digital photo of $V_3Nb_{17}O_{50}$@PAN precursor after electrospinning.

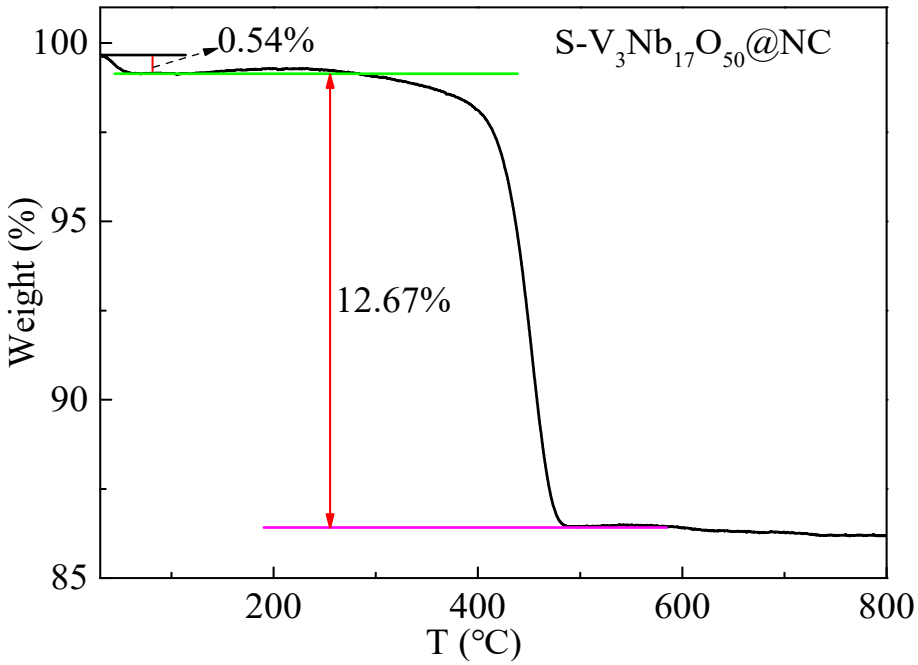

Fig. S2. TGA curve of S-$V_3Nb_{17}O_{50}$@NC.

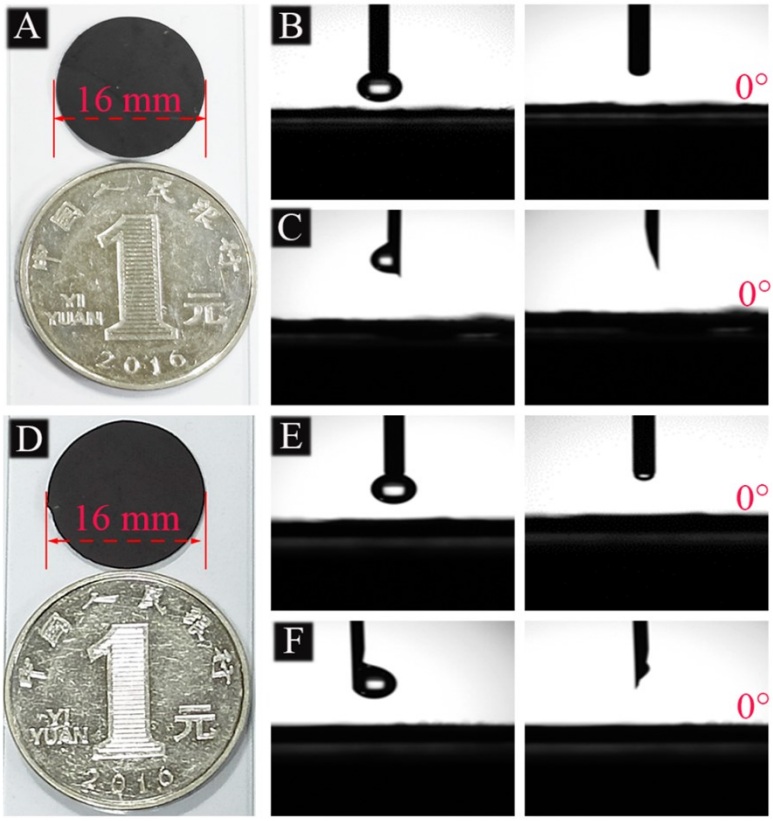

Fig. S3. $V_3Nb_{17}O_{50}$@NC nanofibers plate (A); Contact angle of $V_3Nb_{17}O_{50}$@NC with water (B) and DMC (C); S-$V_3Nb_{17}O_{50}$@NC nanofibers plate (D); Contact angle of S-$V_3Nb_{17}O_{50}$@NC with water (E) and DMC (F).

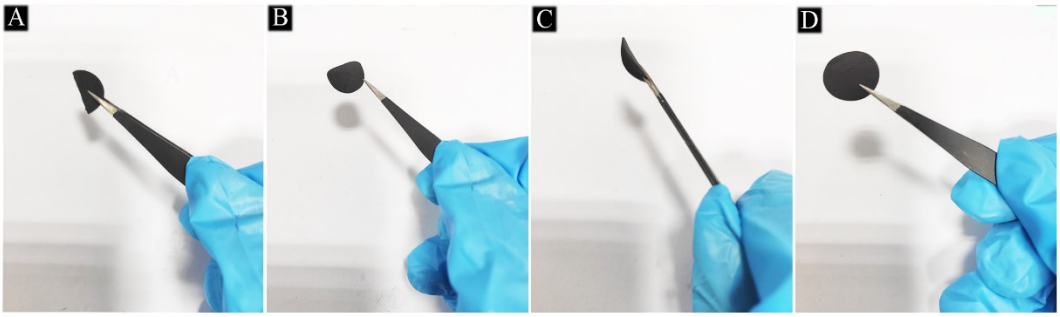

Fig. S4. (A~D) Bending test of S-$V_3Nb_{17}O_{50}$@NC nanofibers.

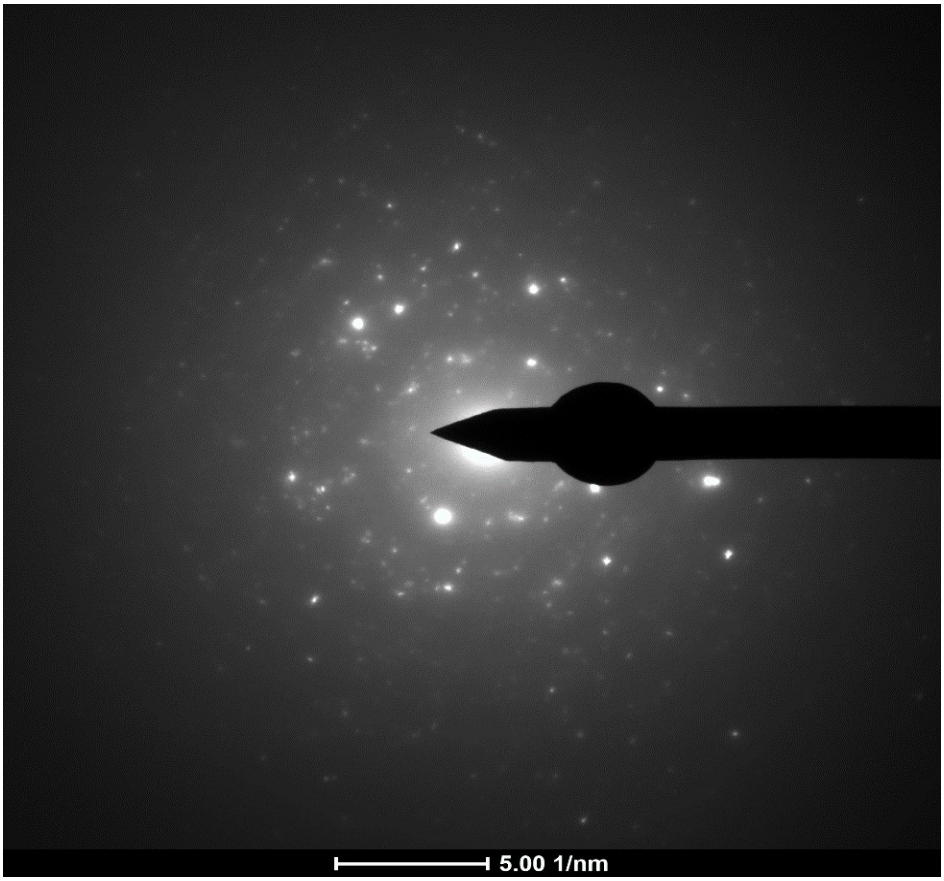

Fig. S5. SAED pattern of S-$V_3Nb_{17}O_{50}$@NC.

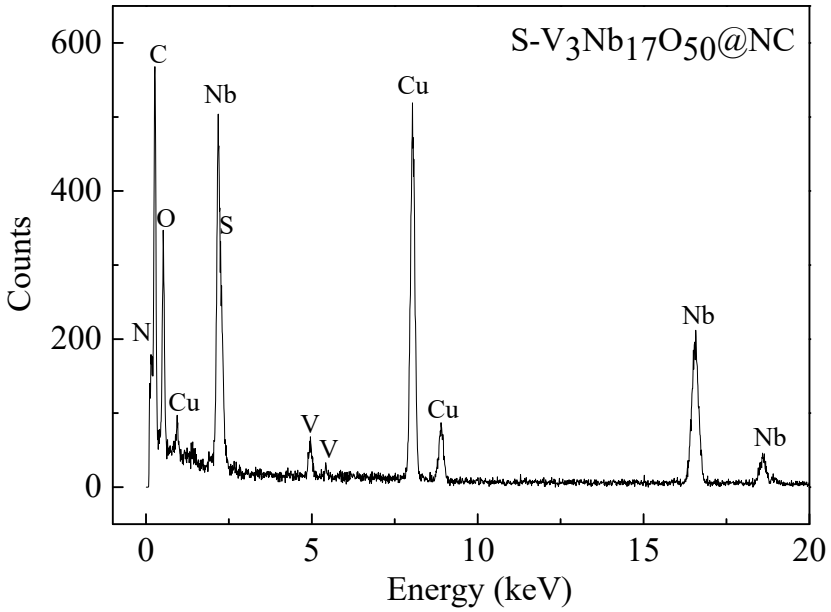

Fig. S6. EDS of S-$V_3Nb_{17}O_{50}$@NC. (Copper element from the TEM matrix.)

Table. S1. Quantification results of S-$V_3Nb_{17}O_{50}$@NC

Element	Weight (%)	Atomic (%)	Uncertainly (%)	Detector Correction	K-Factor
C	37.29	69.43	0.63	0.26	4.032
N	1.71	2.73	0.16	0.26	3.903
O	10.07	14.08	0.26	0.49	2.008
S	2.47	1.72	0.13	0.93	1.015
V	1.83	0.80	0.07	0.99	1.257
Nb	46.6	11.21	0.61	0.99	3.705

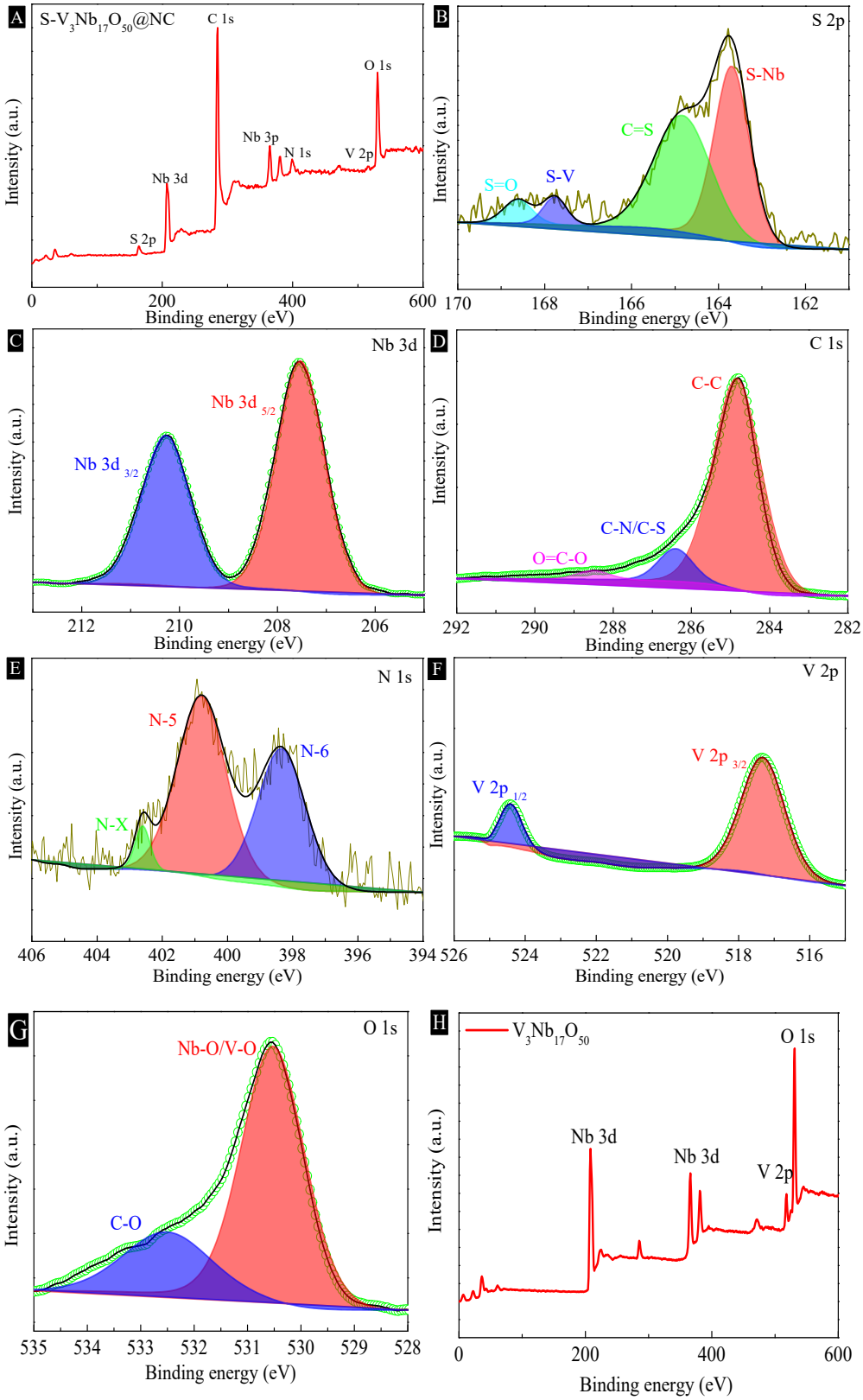

Fig. S7. XPS spectra of S-$V_3Nb_{17}O_{50}$@NC: (A) Scanning spectrum; (B) S 2p; (C) Nb 3d; (D) C 1s; (E) N 1s; (F) V 2p and (G) O 1s. Scanning spectrum of $V_3Nb_{17}O_{50}$ (H).

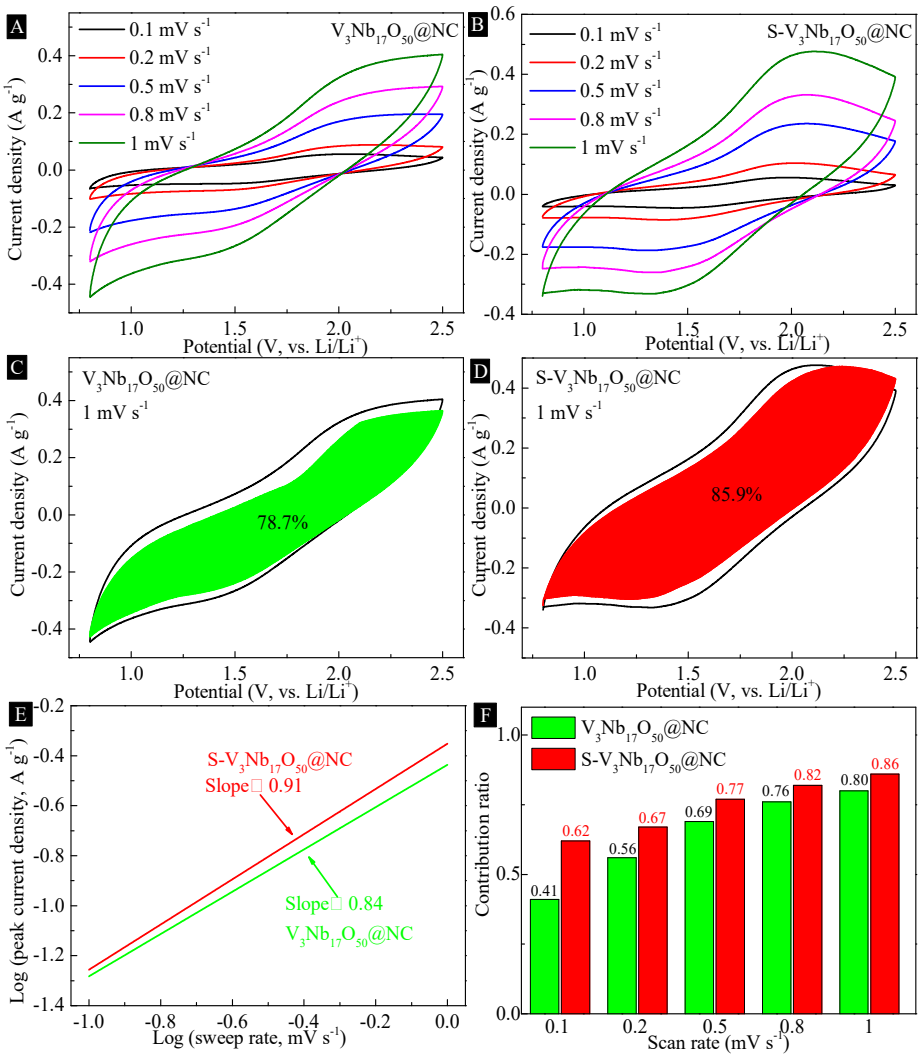

Fig. S8. CV curves of $V_3Nb_{17}O_{50}$@NC (A) and S-$V_3Nb_{17}O_{50}$@NC (B) at scanning rates from 0.1 to 1 mV s^{-1}; Total current (solid line) and capacitive current (shaded part) of $V_3Nb_{17}O_{50}$@NC (C) and S-$V_3Nb_{17}O_{50}$@NC (D) at 1 mV s^{-1}; (E) Relationship between scanning rate and peak current density to calculate b value; (F) Contribution ratio of capacitance and diffusion control processes at various scanning rates.

The dynamic behavior of the sample is studied by the relationship between current (i) and scan rate (v):

$$i = av^b \quad (1)$$

To gain b value, the formula (1) is converted (1) into (2):

$$\log(i) = b\log(v) + \log(a) \quad (2)$$

where a and b are adjustable parameters. The b value, the key parameter to distinguish capacitive-controlled behavior and diffusion-controlled behavior, can be obtained from a linear relationship between log(i) and log(v). Specifically, b≈1 demonstrates the dominance of capacitive controlled process, while b≈0.5 shows the ruling diffusion-

controlled process. The b values of $V_3Nb_{17}O_{50}$@NC and S-$V_3Nb_{17}O_{50}$@NC (Fig. S8E) are 0.84 and 0.91 individually, proving the higher capacitance contribution of the latter (Fig. S8F). Obviously, the defects from N, S co-doping widen the Li^+ transmission channel and boost the ion/electron transmission rate. To further quantify the capacitance contribution ratio, the total current can be divided into capacitive current ($k_1 v$) and diffusion current ($k_2 v^{1/2}$) as follows:

$$i = k_1 v + k_2 v^{1/2} \quad (3)$$

where k_1 and k_2 represent the ratio of capacitive control and diffusive control at fixed potentials. At the current density of 1 mV s^{-1}, the capacitance contribution ratio of $V_3Nb_{17}O_{50}$@NC and S-$V_3Nb_{17}O_{50}$@NC are 78.7% (Fig. S8C) and 85.9% (Fig. S8D) respectively, illustrating the larger capacitance reactivity of S-$V_3Nb_{17}O_{50}$@NC. With the rise of the scan rate, the capacitance contribution ratio of the electrode materials gradually increases (Fig. S8F). From the CV curve (integrated area) and capacitance contribution ratio, the S-$V_3Nb_{17}O_{50}$@NC electrode supplies superior electrochemical performance. Accordingly, the N, S co-doping is helpful to expand lattice channels, provide more reactive sites, and accelerate the lithium-ion transport dynamics.

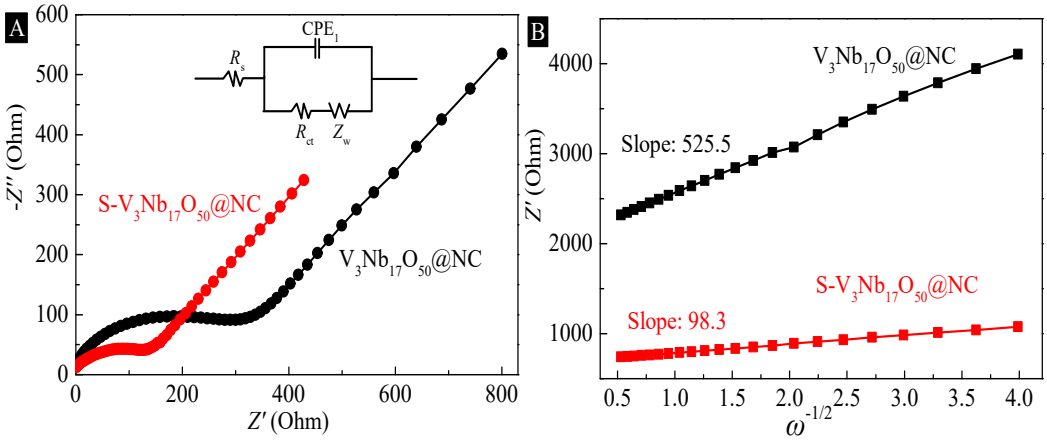

Fig. S9. (A) Impedance spectra of $V_3Nb_{17}O_{50}$@NC and S-$V_3Nb_{17}O_{50}$@NC electrode; (B) Warburg impedance coefficient (σ) from the linear fitting line of Z' versus $\omega^{-1/2}$.

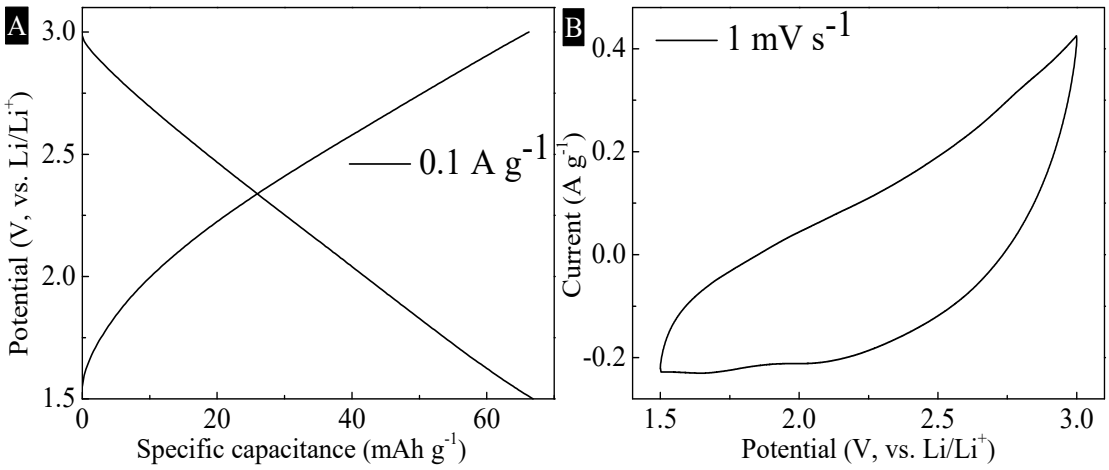

Fig. S10. GCD curves (A) and CV curves (B) of AC//Li.

The energy density and power density of S-$V_3Nb_{17}O_{50}$@NC//AC were achieved by the following formulas:

$$C = \frac{I \times t}{(V_{max} - V_{min}) \times m} \tag{1}$$

$$E = \int_{t_1}^{t_2} IV\mathrm{d}t = \frac{1}{2} C(V_{max} + V_{min})(V_{max} - V_{min}) = \frac{V_{max} + V_{min}}{2} \times \frac{I \times t}{m} \times \frac{1}{3.6} \tag{2}$$

$$P = \frac{3600 \times E}{t} \tag{3}$$

where V_{max} (3.0 V) and V_{min} (0.5 V) are the initial and final discharge potentials (V), I is the discharge current (A), t is the discharge time (s), m is the total mass of the active materials in both anode and cathode (g), C is the specific capacitance (F g^{-1}), E is the energy density (Wh kg^{-1}), and P is the power density (W kg^{-1}).

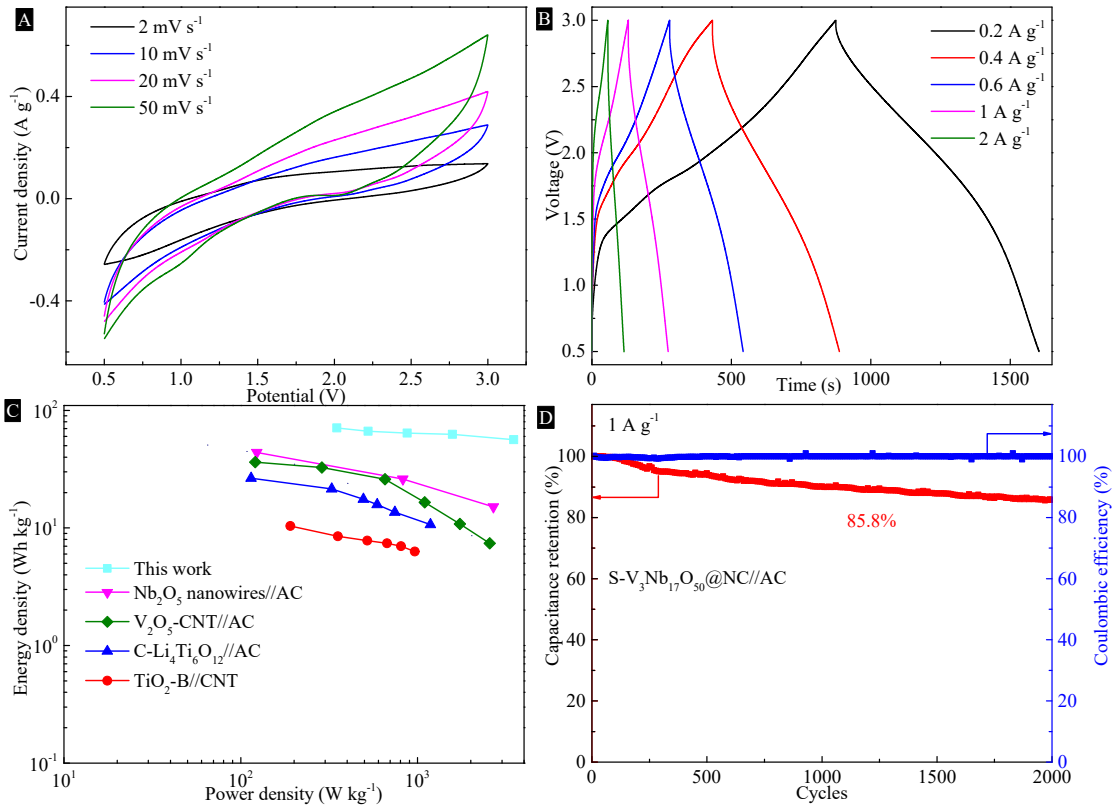

Fig. S11. CV curves (A); GCD curves (B); Ragone plots (C); (D) Cycling performance and Coulombic efficiency at 1 A g^{-1}.

The diffusion coefficient of lithium-ion (D_{Li}) can be further calculated from the low-frequency region according to the following formula:

$$D_{Li} = \frac{(RT)^2}{2A^2n^4F^4C_{Li}^2\sigma^2} \quad (4)$$

$$Z' = R_{ct} + R_s + \sigma\omega^{-1/2} \quad (5)$$

where R is the gas constant, T is the absolute temperature (K), A is the surface area of the electrode (cm^2), n is the electrons number per molecule in the intercalation

process, F is the Faraday constant, C_{Li} is the Li^+ molar concentration in electrode (mol L^{-1}), ω is the angular frequency, and σ is the Warburg factor related with Z'. In addition, the σ can be obtained by linearly fitting Z' with $\omega^{-1/2}$. D_{Li} is acquired by substituting different values of σ (Fig. S9B) into equation (4). From the calculation results, the D_{Li} of S-$V_3Nb_{17}O_{50}$@NC (1.16×10^{-7} cm^2 s^{-1}) is larger than that of $V_3Nb_{17}O_{50}$@NC (2.18×10^{-8} cm^2 s^{-1}), which proves that N, S co-doping endows S-$V_3Nb_{17}O_{50}$@NC with good conductivity and ion mobility.

Based on the good electrochemical performance of S-$V_3Nb_{17}O_{50}$@NC with lithium foil electrode in half battery, its application in lithium-ion hybrid capacitor (LIC) was further studied. Herein, the assembled LIC as an energy storage device combine Li^+-intercalation Faraday reaction (S-$V_3Nb_{17}O_{50}$@NC) with ion adsorption/desorption non-Faraday reaction (AC). To maximize the energy storage capacity, the working voltage range and the mass ratio of S-$V_3Nb_{17}O_{50}$@NC anode to AC cathode need to be optimized. According to the specific capacity at the same current density, the optimum mass ratio of two electrodes was calculated to be 1:3.6 using the charge conservation law ($C_+ \times E_+ \times m_+ = C_- \times E_- \times m_-$). The voltage range was carefully determined to be 0.5 V to 3 V. The electrochemical performance of AC electrode was also tested in a half-cell with AC as cathode and Li as anode. As for CV curve, the AC electrode at a scan rate of 1 mV s^{-1} (Fig. S10B) shows the typical characteristics of double-layer capacitance, along with highly symmetric triangles (vs. Li/Li^+) in the GCD curve (Fig. S10A). The CV (Fig. S11A) and GCD (Fig. S11B) curves of the LIC (S-$V_3Nb_{17}O_{50}$@NC//AC) do not appear typically rectangular and triangular, owning to the coupling of pseudo-capacitive intercalation and surface adsorption behavior. During the discharge process, Li^+ is de-embedded from S-$V_3Nb_{17}O_{50}$@NC, accompanied by the PF^{6-} desorption from AC surface. While for the charge process, the reaction is reversed. S-$V_3Nb_{17}O_{50}$@NC//AC (Fig. S11D), retaining a specific capacitance of 85.8% after 2000 cycles at a current density of 1 A g^{-1}, with nearly 100% Coulombic efficiency, demonstrate good cycling stability.

The crystal plane spacing of $V_3Nb_{17}O_{50}$ and $V_3Nb_{17}O_{50}$ @NC was analyzed by HRTEM (Fig. S12). The crystal plane spacing of $V_3Nb_{17}O_{50}$ (Fig. S12A), $V_3Nb_{17}O_{50}$@NC (Fig. S12B), S-$V_3Nb_{17}O_{50}$@NC (Fig. 2H) are 0.316 nm, 0.348 nm, 0.367 nm, respectively, indicating that the crystal plane spacing of $V_3Nb_{17}O_{50}$ is widened after N and S doping.

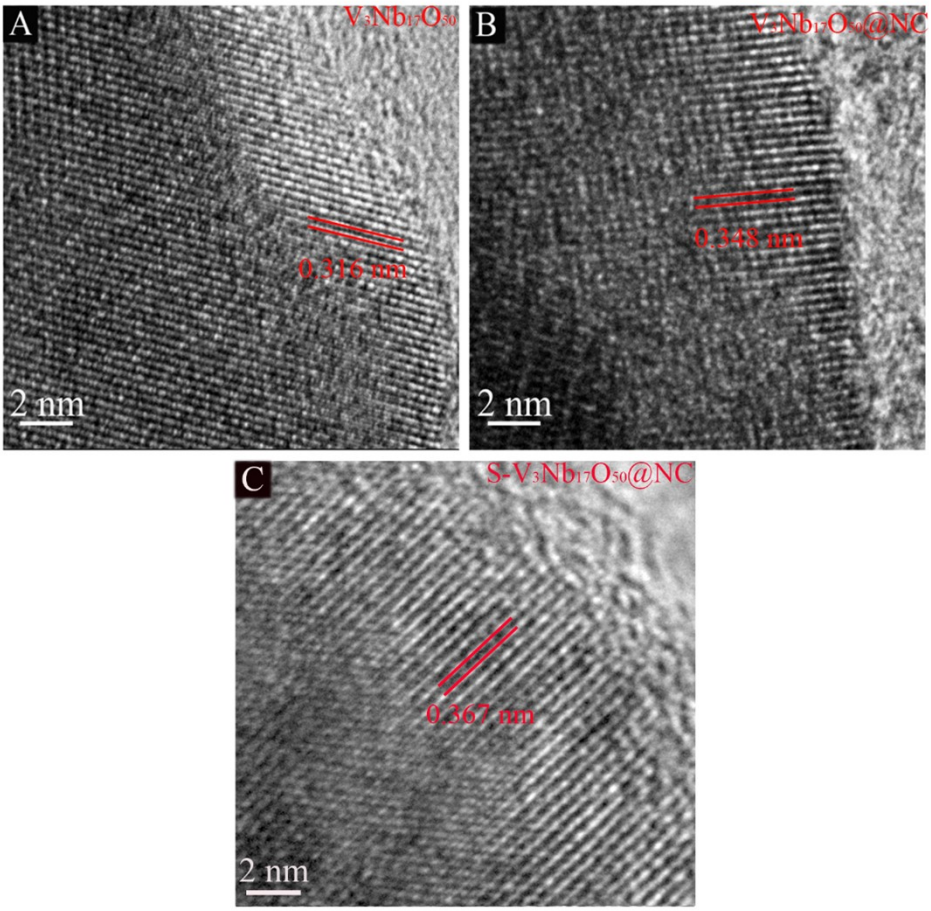

Fig. 12. HRTEM images of $V_3Nb_{17}O_{50}$ (A), $V_3Nb_{17}O_{50}$@NC (B), and S-$V_3Nb_{17}O_{50}$@NC (C).

The specific surface area and pore size distribution of S-$V_3Nb_{17}O_{50}$@NC were analyzed by N_2 adsorption analyzer (BET). From BET information, a large S_{BET} (78.4 $m^2\ g^{-1}$) and a good mesoporous size distribution (centred at 10 nm) of S-$V_3Nb_{17}O_{50}$@NC (Fig. S13) are achieved, which is helpful to accelerate Li^+ diffusion and provide more electroactive sites.

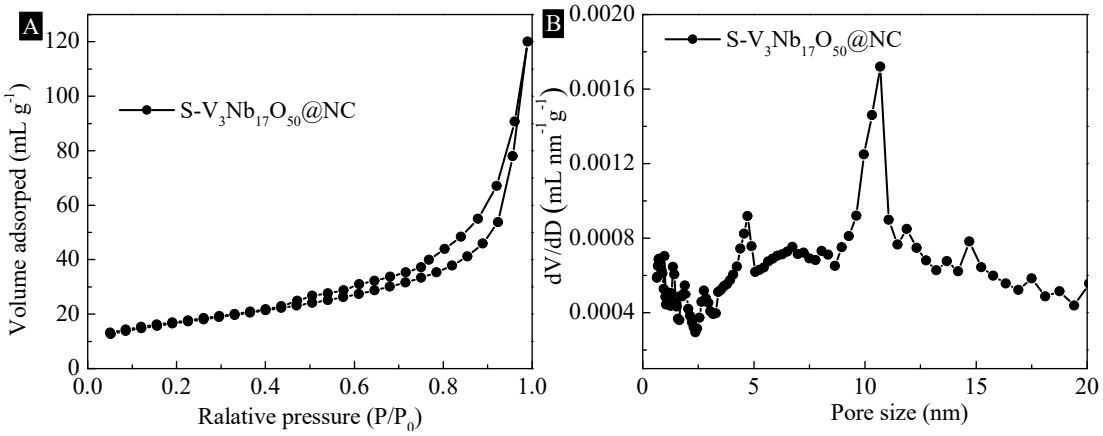

Fig. S13. BET adsorption isotherms (A) and pore size distribution (B) of S-$V_3Nb_{17}O_{50}$@NC.

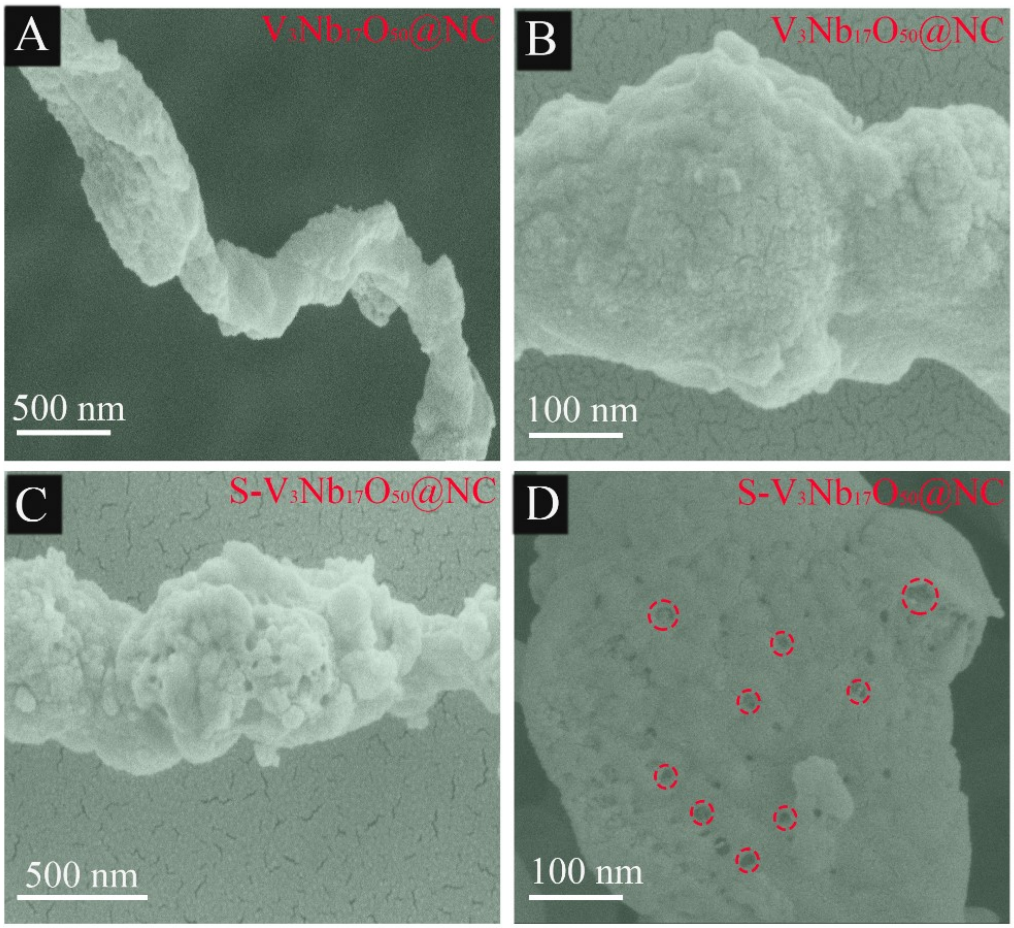

Fig. S14. SEM of $V_3Nb_{17}O_{50}$@NC (A and B) and S-$V_3Nb_{17}O_{50}$@NC (C and D).

The GCD curves of $V_3Nb_{17}O_{50}$, $V_3Nb_{17}O_{50}$@NC, and S-$V_3Nb_{17}O_{50}$@NC (Fig. S15) were tested at 0.1 A g^{-1} current density. Specifically, the $V_3Nb_{17}O_{50}$, $V_3Nb_{17}O_{50}$@NC, and S-$V_3Nb_{17}O_{50}$@NC display reversible capacity of 163.4 mAh g^{-1}, 186.4 mAh g^{-1}, and 221.2 mAh g^{-1}, respectively. Compared with $V_3Nb_{17}O_{50}$, $V_3Nb_{17}O_{50}$@NC increases by 23 mAh g^{-1}, while S-$V_3Nb_{17}O_{50}$@NC rising 58.7 mAh g^{-1}, indicating sulfur vapor etching produces advanced porous structure and large specific surface area of S-$V_3Nb_{17}O_{50}$@NC, which is conducive to Li^+ transport dynamics.

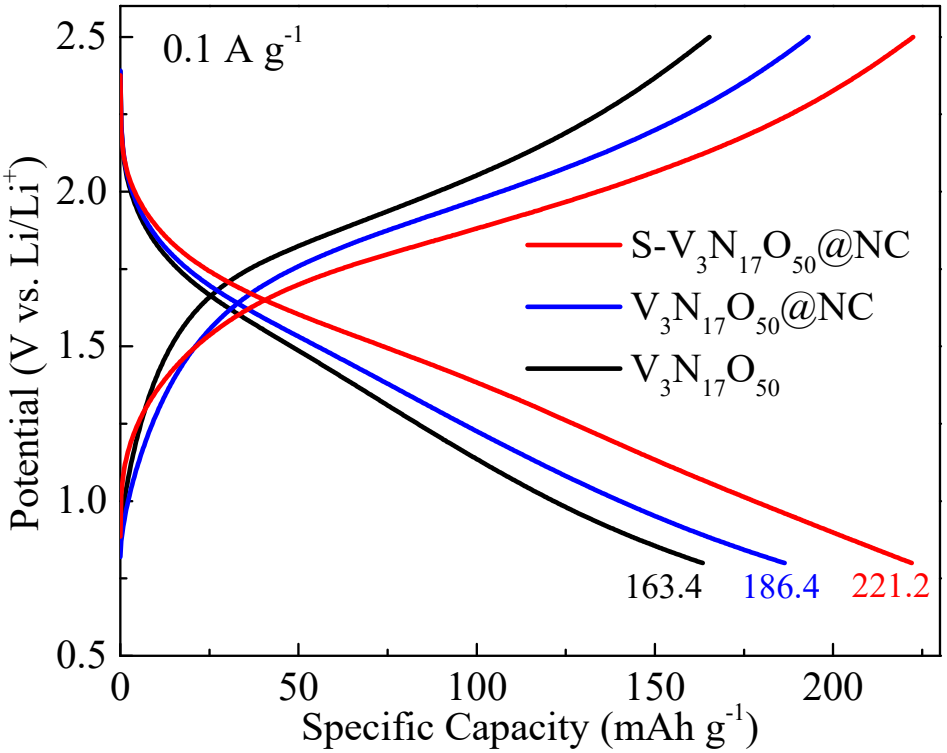

Fig. S15. GCD curves of $V_3Nb_{17}O_{50}$, $V_3Nb_{17}O_{50}$@NC and S-$V_3Nb_{17}O_{50}$@NC at 0.1 A g^{-1}.

GCD curves and time-capacity curves of $V_3Nb_{17}O_{50}$, $V_3Nb_{17}O_{50}$@NC, and S-$V_3Nb_{17}O_{50}$@NC were tested at 5 A g^{-1} current density (Fig. S16). Specifically, the reversible specific capacity of $V_3Nb_{17}O_{50}$, $V_3Nb_{17}O_{50}$@NC, and S-$V_3Nb_{17}O_{50}$@NC are 38.7 mAh g^{-1}, 51.2 mAh g^{-1}, and 84.8 mAh g^{-1}, respectively. Meanwhile, when the reversible specific capacity reaches 38.7 mAh g^{-1}, the charging time required for $V_3Nb_{17}O_{50}$, $V_3Nb_{17}O_{50}$@NC and S- $V_3Nb_{17}O_{50}$@NC is 30.02 s, 27.98 s and 25.73 s, individually, indicating that the N, S co-doping enhances the conductivity and provides more active sites to increase capacitance performance.[1,2,3]

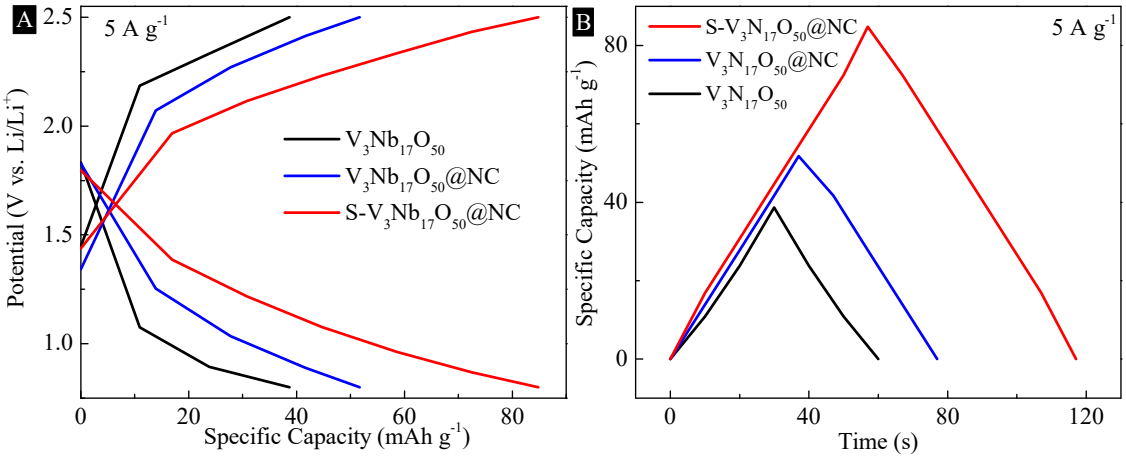

Fig. S16. GCD curves and time-capacity curves at 5 A g^{-1}.

To further illustrate the carbon layer effect, the GCD curves of initial three cycles for $V_3Nb_{17}O_{50}$ and S-$V_3Nb_{17}O_{50}$@NC are supplemented (Fig. S17). In detail, the first charge/discharge cycle of $V_3Nb_{17}O_{50}$ delivers specific capacity of 176.3/220.6 mAh g^{-1} with a low initial cycle Coulombic efficiency (79.9%). Relatively, S-$V_3Nb_{17}O_{50}$ @NC shows high specific capacity (228.8/235.7 mAh g^{-1}) and initial Coulombic efficiency (97.1%), verifying the improved Li^+ transport efficiency. Specifically, the retention of Li^+ in the $V_3Nb_{17}O_{50}$ lattice and SEI layer formation leads to lattice blockage, thus lowering $V_3Nb_{17}O_{50}$ specific capacity.[4] Meanwhile, the amorphous carbon layer, as a SEI layer to some extent, can provide more Li^+ transport channels, lessen excessive Li^+ entering $V_3Nb_{17}O_{50}$ lattice, and boost the Li^+ transport uniformity and stability.[5,6,7]

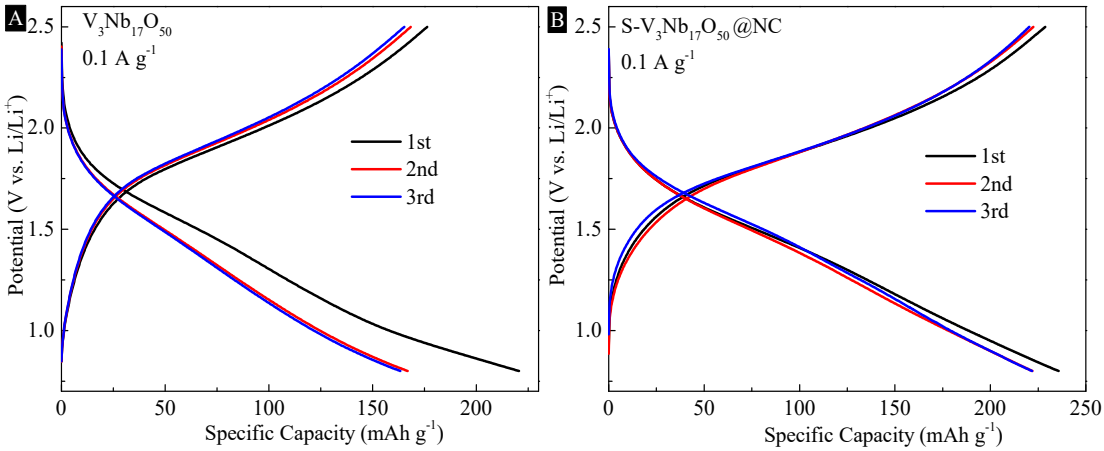

Fig. S17 GCD curves of $V_3Nb_{17}O_{50}$ (A) and S-$V_3Nb_{17}O_{50}$@NC (B) at 0.1 A g^{-1}.

Table. S2. Theoretical capacity of bimetallic niobium oxide

Sample	Theoretical capacity (mAh g^{-1})	References
This work	423	
$TiNb_2O_7$	387	8
$Ti_2Nb_{10}O_{29}$	396	9
$FeNb_{11}O_{29}$	400	10
$CrNb_{11}O_{29}$	401	11
$AlNb_{11}O_{29}$	390	12
$GaNb_{11}O_{29}$	379	13
$Mg_2Nb_{34}O_{87}$	396	14
$Zn_2Nb_{34}O_{87}$	389	15
$Cu_2Nb_{34}O_{87}$	401	16
$AgNb_{13}O_{33}$	377.9	17
$MoNb_{12}O_{33}$	401	18
$ZrNb_{14}O_{37}$	378.3	19
$HfNb_{24}O_{62}$	378	20

References:

1 X. Li, X. Hu, L. Zhou, R. Wen, X. Xu, S. Chou, L. Chen, A.-M. Cao and S. Dou, *J. Mater. Chem. A*, 2019, **7**, 11976–11984.

2 Z. Lu, Y. Zhai, N. Wang, Y. Zhang, P. Xue, M. Guo, B. Tang, D. Huang, W. Wang, Z. Bai and S. Dou, *Chem. Eng. J.*, 2020, **380**, 122455.

3 W. Gou, X. Kong, Y. Wang, Y. Ai, S. Liang, A. Pan and G. Cao, *Chem. Eng. J.*, 2019, **374**, 545–553.

4 Q. Fu, X. Zhu, R. Li, G. Liang, L. Luo, Y. Chen, Y. Ding, C. Lin, K. Wang and X. S. Zhao, *Energy Storage Mater.*, 2020, **30**, 401–411.

5 L. Chen, J. Zhang, R. Tong, J. Zhang, H. Wang, G. Shao and C. Wang, *Small*, 2022, **18**, 2106142.

6 Y. Lian, Y. Zheng, D. Wang, Y. Bai, H. Yan, Z. Wang, J. Zhao and H. Zhang, *J. Colloid Interface Sci.*, 2022, **606**, 77–86.

7 H.-S. Lim, Y.-K. Sun and K.-D. Suh, *J. Mater. Chem. A*, 2013, **1**, 10107.

8 Y. Huang, X. Li, J. Luo, K. Wang, Q. Zhang, Y. Qiu, S. Sun, S. Liu, J. Han and Y. Huang, *ACS Appl. Mater. Interfaces*, 2017, **9**, 8696–8703.

9 J. Zeng, L. Yang, R. Shao, L. Zhou, W. Utetiwabo, S. Wang, R. Chen and W. Yang, *J. Colloid Interface Sci.*, 2021, **600**, 111–117.

10 R. Zheng, S. Qian, X. Cheng, H. Yu, N. Peng, T. Liu, J. Zhang, M. Xia, H. Zhu and J. Shu, *Nano Energy*, 2019, **58**, 399–409.

11 Q. Fu, X. Liu, J. Hou, Y. Pu, C. Lin, L. Yang, X. Zhu, L. Hu, S. Lin, L. Luo and Y. Chen, *J. Power Sources*, 2018, **397**, 231–239.

12 X. Lou, R. Li, X. Zhu, L. Luo, Y. Chen, C. Lin, H. Li and X. S. Zhao, *ACS Appl. Mater. Interfaces*, 2019, **11**, 6089–6096.

13 X. Lou, Q. Fu, J. Xu, X. Liu, C. Lin, J. Han, Y. Luo, Y. Chen, X. Fan and J. Li, *ACS Appl. Nano Mater.*, 2018, **1**, 183–190.

14 X. Zhu, Q. Fu, L. Tang, C. Lin, J. Xu, G. Liang, R. Li, L. Luo and Y. Chen, *ACS Appl. Mater. Interfaces*, 2018, **10**, 23711–23720.

15 X. Zhu, H. Cao, R. Li, Q. Fu, G. Liang, Y. Chen, L. Luo, C. Lin and X. S. Zhao, *J. Mater. Chem. A*, 2019, **7**, 25537–25547.

16 X. Cai, H. Yan, Z. Yang, J. Zhang, H. Yu, L. Zhang and J. Shu, *Ceram. Int.*, 2021, **47**, 24511–24518.

17 Z. Chen, X. Cheng, W. Ye, R. Zheng, H. Zhu, H. Yu, N. Long, M. Shui and J. Shu, *Chem. Eng. J.*, 2019, **366**, 246–253.

18 X. Zhu, J. Xu, Y. Luo, Q. Fu, G. Liang, L. Luo, Y. Chen, C. Lin and X. S. Zhao, *J. Mater. Chem. A*, 2019, **7**, 6522–6532.

19 Y. Li, R. Zheng, H. Yu, X. Cheng, T. Liu, N. Peng, J. Zhang, M. Shui and J. Shu, *ACS Appl. Mater. Interfaces*, 2019, **11**, 22429–22438.

20 Q. Fu, H. Cao, G. Liang, L. Luo, Y. Chen, V. Murugadoss, S. Wu, T. Ding, C. Lin and Z. Guo, *Chem. Commun.*, 2020, **56**, 619–622.